

Computed versus measured ion velocity distribution functions in a Hall effect thruster

L. Garrigues, S. Mazouffre, and G. Bourgeois

Citation: *J. Appl. Phys.* **111**, 113301 (2012); doi: 10.1063/1.4722269

View online: <http://dx.doi.org/10.1063/1.4722269>

View Table of Contents: <http://jap.aip.org/resource/1/JAPIAU/v111/i11>

Published by the [American Institute of Physics](#).

Related Articles

Rotation of tokamak halo currents

Phys. Plasmas **19**, 052508 (2012)

Impact of screening of resonant magnetic perturbations in three dimensional edge plasma transport simulations for DIII-D

Phys. Plasmas **19**, 052507 (2012)

Energy spectrum, dissipation, and spatial structures in reduced Hall magnetohydrodynamic

Phys. Plasmas **19**, 052305 (2012)

Suppressing electron turbulence and triggering internal transport barriers with reversed magnetic shear in the National Spherical Torus Experiment

Phys. Plasmas **19**, 056120 (2012)

Magnetohydrodynamic spin waves in degenerate electron-positron-ion plasmas

Phys. Plasmas **19**, 052101 (2012)

Additional information on J. Appl. Phys.

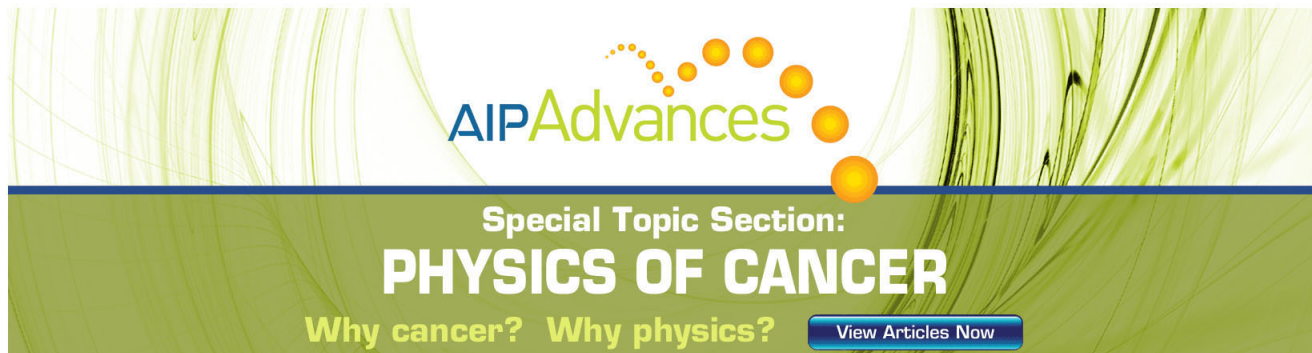
Journal Homepage: <http://jap.aip.org/>

Journal Information: http://jap.aip.org/about/about_the_journal

Top downloads: http://jap.aip.org/features/most_downloaded

Information for Authors: <http://jap.aip.org/authors>

ADVERTISEMENT



AIP Advances

Special Topic Section:
PHYSICS OF CANCER

Why cancer? Why physics? [View Articles Now](#)

Computed versus measured ion velocity distribution functions in a Hall effect thruster

L. Garrigues,^{1,2,a)} S. Mazouffre,³ and G. Bourgeois³

¹Université de Toulouse, UPS, INPT, LAPLACE (Laboratoire Plasma et Conversion d'Énergie), 118 route de Narbonne, F-31062 Toulouse cedex 9, France

²CNRS, LAPLACE, F-31062 Toulouse, France

³ICARE (Institut de Combustion, Aérodynamique, Réactivité et Environnement), 1 C avenue de la recherche scientifique, 45071 Orléans, France

(Received 30 January 2012; accepted 24 April 2012; published online 1 June 2012)

We compare time-averaged and time-varying measured and computed ion velocity distribution functions in a Hall effect thruster for typical operating conditions. The ion properties are measured by means of laser induced fluorescence spectroscopy. Simulations of the plasma properties are performed with a two-dimensional hybrid model. In the electron fluid description of the hybrid model, the anomalous transport responsible for the electron diffusion across the magnetic field barrier is deduced from the experimental profile of the time-averaged electric field. The use of a steady state anomalous mobility profile allows the hybrid model to capture some properties like the time-averaged ion mean velocity. Yet, the model fails at reproducing the time evolution of the ion velocity. This fact reveals a complex underlying physics that necessitates to account for the electron dynamics over a short time-scale. This study also shows the necessity for electron temperature measurements. Moreover, the strength of the self-magnetic field due to the rotating Hall current is found negligible. © 2012 American Institute of Physics. [<http://dx.doi.org/10.1063/1.4722269>]

I. INTRODUCTION

Hall effect thrusters (HETs) are gridless ion sources used onboard telecommunication satellites mainly for station keeping and attitude control.^{1,2} Doppler-shifted laser-induced-fluorescence (LIF) technique is currently employed to characterize atom and ion species velocity in HETs. This technique is non-intrusive that means the ion and atom velocity distribution functions (VDF) can be captured without disturbing the thruster discharge. Time-averaged ion (e.g., Refs. 3–7) and neutral (Refs. 4 and 8) VDFs have extensively been measured in a variety of thrusters in the past few years. The time-evolution of the axial ion VDFs has recently been achieved using a pulse-counting detection technique.⁹ From the measured ion velocity profile, which is obtained either from the most probable velocity or from the mean velocity, one can deduce the accelerating electric field distribution assuming that the ionization takes place upstream the acceleration region.^{3,5–7} In most of HET working conditions, this assumption is, however, not valid since the ionization and acceleration layers overlap.¹⁰ A method that does not require any assumptions was therefore proposed. The accelerating electric field and ionization source term profiles (number of ions created by units of time and volume) can be derived from the measured ion VDFs taking moments of Boltzmann equation. This method has been originally proposed for one-dimensional configurations¹¹ and recently extended to the 2D calculation of the electric field.¹² Unfortunately, for time-varying data, the method based on the resolution of the Boltzmann equation is not applicable on a practical

viewpoint due to noise spreading and amplification during high order moments calculation.⁹ However, the LIF measurements of ion VDFs combined with the Boltzmann equation is by far the most powerful technique that can be used to help for numerical model validation.

To simulate the HET operation, various transient numerical models have been developed, in one-axial dimension with hybrid¹³ and fluid¹⁴ approaches, in two-axial-radial dimensions by means of hybrid^{15–21} and particle-in-cell (PIC) with scaling factors^{22–24} techniques, and in two-axial-azimuthal dimensions using PIC approach.²⁵ The hybrid approach, in which the electrons are treated as a collisional-fluid assuming an isotropic Maxwellian VDF and the heavy species are treated with a non-collisional fluid or using particle methods, is the most common method for modelling a HET discharge. The advantages of this technique, combined with the quasineutrality assumption, are related to the short computational time and easiness to perform parametric studies. The drawback of a fluid description of the electrons is the approximate treatment of the electron transport across the magnetic field lines. Due to the intense ionization of the neutral flow, the diffusion of the electrons across the magnetic field barrier cannot be explained by classical collisional phenomenon. The electron magnetic field cross-diffusion needs to be enhanced taking into account non-classical processes such as electron-wall collisions (originally proposed by Morozov and Savelyev²⁶ under the “near-wall conductivity” theory) and/or plasma turbulence. The induced electron transport due to non-classical processes is often referred to as “anomalous” transport in the literature, in contrast with the “classical” transport due to collisions. Nevertheless, the so far developed 2D hybrid models fail to self-consistently

^{a)}Electronic mail: laurent.garrigues@laplace.univ-tlse.fr.

account for non-classical phenomena for several reasons. First, a complete theory of electron-wall collisions requires to know the electron VDF shape that is *a priori* assumed in fluid approach. Second, the electron-wall collision theory cannot be an explanation for the electron transport outside the channel. Third, the hybrid model we have developed does not account for the azimuthal direction along which a fluctuating electric field is responsible for the electron diffusion (e.g., Refs. 25 and 27). Only a complete but time consuming and not yet available 3D PIC model would be able to predict the electron transport across the magnetic field barrier in HETs.

In 2D hybrid models, the solution generally adopted is to enhance electron-heavy particle collision frequencies with additional collision frequencies representing non-classical processes using time-constant empirical coefficients.^{13,15,18,19} The empirical coefficients are tuned in order to reproduce experimental features like thruster performance, discharge current, and so on. Recent studies have nevertheless demonstrated that the use of empirical laws fails to reproduce the measured potential and ion velocity profiles.^{16,17,28,29} Since the electron transverse mobility cannot be described with simple laws, Garrigues and co-workers,²⁸ and Adam and co-workers,²⁹ have proposed to adjust it in order that the simulated electric field profile matches the measured one. A time-independent electron transverse mobility axial profile has then been proposed for a 1.5 and a 5 kW-class HET.^{28,29} In this paper, we analyse the limit of using a time-independent anomalous mobility profile through a detailed comparison between time-averaged and time-varying computed and measured ion VDFs for the 1.5 kW-class PPS[®]100-ML thruster. The PPS[®]100-ML thruster was already described in Refs. 6 and 8. The optical bench for LIF measurements has been explained in details in Refs. 6 and 7. The photon-counting technique together with the associated procedure for time-resolved measurements have been extensively discussed in Ref. 9.

We briefly describe the 2D hybrid model in Sec. II. Section III is dedicated to the detailed comparisons between measured and computed plasma and ion properties first in a time-averaged mode and then in a time-varying mode. The possible influence of the magnetic field induced by the Hall current is also examined. Finally, Sec. IV summarizes the main results of this work.

II. DESCRIPTION OF THE TWO-DIMENSIONAL HYBRID MODEL

The 2D (axial-radial) hybrid model has been described in details elsewhere.¹⁵ Here, we only provide the basis of the numerical model. The magnetic field profile is computed separately from the thruster geometry and the positions of all the magnetic elements. The computational domain starts at the anode plane and ends at the magnetic field line intercepting the cathode. We consider that the plasma is quasineutral; sheaths are not described. The plasma density n is inferred from the kinetic description of the ion transport. The electron fluid equations are derived from the first three moments of the Boltzmann's equation. The particularity of HETs is that the

electron transport along the magnetic field lines is not impeded by the magnetic field, while the transverse electron transport is reduced by the Hall parameter squared h^2 , wherein $h = \omega/\nu$, ω and ν being the cyclotron pulsation and collision frequency, respectively. In the region of strong magnetic field magnitude, $h > 100$. The electrons can therefore be considered in Boltzmann equilibrium along the magnetic field lines, and the electric potential V can be written as:²⁶

$$V = V^* + \frac{k_B T_e}{e} \ln\left(\frac{n}{n_0}\right). \quad (1)$$

In Eq. (1), V^* is a function depending on the magnetic field lines, k_B is Boltzmann constant, e is the elementary charge, n_0 is a reference plasma density, and T_e is the electron temperature. In Eq. (1), V and n depend on the spatial coordinates, while V^* and T_e are uniform along the magnetic field lines. The electric potential in Eq. (1) is calculated from a generalized Ohm's law where we assume that the electron momentum equation reduced to the drift-diffusion equation.¹⁵ The electron VDF is assumed to be Maxwellian. The electron temperature involved in Eq. (1) and in the calculation of the ionization source term profile is determined from the resolution of an energy equation. The energy equation includes conductive and convective terms, Joule heating, energy losses in inelastic collisions (disregarding losses in elastic collisions), and energy losses due to secondary electron emission (SEE) under electron impacts on the channel walls in a phenomenological way. The energy equation reads:

$$\frac{\partial(n\varepsilon)}{\partial t} + \frac{5}{3} \nabla \cdot [\Gamma_e \varepsilon] - \frac{10}{9} \nabla \cdot [n\mu\varepsilon \nabla \varepsilon] = -eE\Gamma_e - Nn\kappa - nW. \quad (2)$$

In Eq. (2), ε is the electron mean energy ($\varepsilon = 3/2k_B T_e$), Γ_e is the electron flux, μ is the cross-magnetic field mobility, E is the electric field, N is the neutral density, κ is the energy inelastic loss coefficient (tabulated as a function of ε), and W is an effective energy loss coefficient due to electron-wall collisions. The electron energy distribution function (EEDF) is assumed to be Maxwellian. The relation between W and ε is:

$$W = \alpha_e 10^7 \varepsilon \exp\left[-\frac{U}{\varepsilon}\right], \quad (3)$$

where α_e is a parameter and U is set to 20 eV. More details about the numerical procedure used to solve Eqs. (2) and (3) can be found in Ref. 15.

As already discussed in introduction and based on the works of Refs. 28 and 29, the cross-magnetic field mobility μ is written as the sum of a collisional mobility μ_c and an anomalous mobility μ_{ano} derived from measurements:

$$\mu = \mu_c + \mu_{ano} = \frac{m_e \nu_m}{e B^2} + \mu_{ano}, \quad (4)$$

where m_e is the electron mass and ν_m includes the electron-atom and electron-ion collision frequencies.²⁹

Ions are created according to the calculated 2D ionization source term deduced from spatial profiles of plasma and neutral densities and ionization rate (tabulated as a function of the electron mean energy ε). Only the electric field acts on the ion motions. The magnetic field impact on ion trajectories is neglected due to the large Larmor radius. Ions that hit the walls are neutralized and new atoms are formed. Finally, the transport of neutrals includes the injection of neutral atoms through the gas distributor at the anode plane for given mass flow and distributor temperature, collisions with walls for given accommodation coefficients,⁸ losses inside the discharge volume due to ionization, and creation at the walls due to ion recombination. We also account for a supplementary injection of neutrals at the boundaries of the computational domain to simulate the vacuum chamber backpressure. Charge exchange collisions are taken into account. Cross sections are taken from Ref. 30.

III. RESULTS AND DISCUSSION

All the comparisons between computed and measured quantities have been carried out for the same thruster working conditions: a discharge voltage of $U_d = 250$ V, a xenon anode mass flow rate $m_a = 4.5$ mg s⁻¹, a current in all the coils of 5 A, and a vacuum chamber backpressure of 2.5 mPa. For convenience, in the rest of the paper, the coordinate $x = 0$ mm refers to the channel exit plane. In the calculations, we have recorded the axial ion VDFs at a radial position of 4 mm from the internal wall and at the same axial location used for LIF measurements. As in experiments, the spatial resolution is 0.2 mm.

A. Time-averaged quantities

We have plotted in Fig. 1(a) the measured and calculated time-averaged electric field and ionization source term profiles as a function of axial position along the laser beam axis. The good agreement between the measured and the computed distribution has been obtained by adjusting the anomalous mobility μ_{ano} involved in electron fluid equations. The ionization and acceleration layers overlap are clearly visible. If the peak of the ionization frequency calculated from LIF measurements and from the hybrid model is located 5 mm upstream the exit plane, the magnitude differs by a factor of two. In the experiments, the ionization region is shifted in the direction of the channel exhaust. We have plotted in Fig. 1(b) the axial profiles of the simulated electron mean energy and ion plasma density. The maximum of plasma density reaches 3.5×10^{18} m⁻³ at 1 cm upstream of the exit plane. The highest electron mean energy (60 eV) is localized in the region where electrons are heated by the electric field. At $x = -5$ mm, the electron mean energy decreased to about 20 eV. Assuming a Maxwellian EEDF, the electron mean energy must be 40 eV to reach an ionization frequency of 8×10^5 s⁻¹ (see Fig. 1(b)). We can likely think that the maximum of electron energy exceeds by far 60 eV at the exit plane. A first hypothesis is an underestimation of the electron temperature in the calculations. Another hypothesis concerns the existence of a non Maxwellian EEDF due to plasma instabilities in the channel exhaust

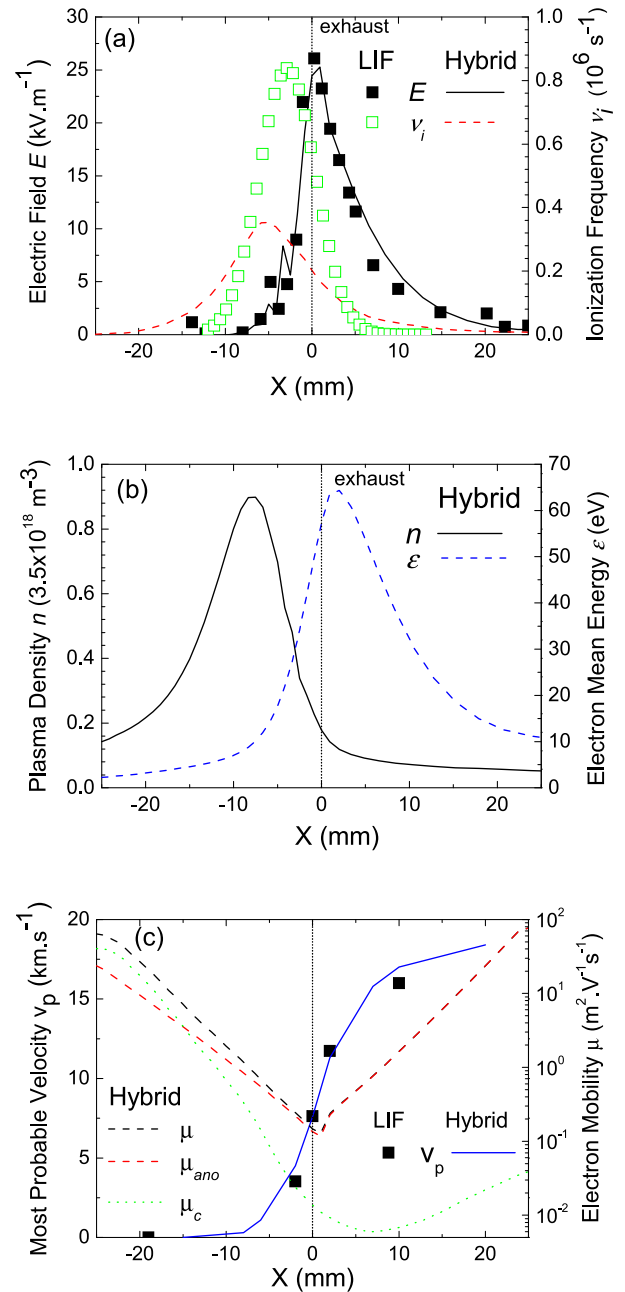


FIG. 1. Time-averaged profiles along the axial position at a radial position of 4 mm from the internal wall of (a) the electric field and ionization frequency deduced from LIF measurements¹⁷ and from the hybrid model, (b) the calculated plasma density and electron mean energy, and (c) the electron mobility perpendicular to the magnetic field and most probable ion velocity measured¹⁷ and calculated. Conditions are: $U_d = 250$ V, $m_a = 4.5$ mg s⁻¹. The backpressure is 2.5 mPa. The coil currents are fixed to 5 A. The channel exit is at $x = 0$ mm.

region.²⁵ In Fig. 1(c), we have also plotted the measured and the calculated most probable velocity v_p profiles. They agree, as expected. We define the most probable velocity as the ion velocity for which the VDF is maximum. The different terms involved in the electron mobility defined in Eq. (4) are displayed in the same figure. The electron mobility μ is governed by the anomalous mobility μ_{ano} behind $x = -15$ mm. The lowest electron mobility (~ 0.2 m² V⁻¹ s⁻¹) corresponds to the maximum of electric field and magnetic field ($x \approx 0$ mm). The collisional mobility μ_c controls the electron

mobility only in the anode region where the neutral density is large. We notice that the electron energy is large enough to ionize the back pressure downstream of the exit plane (see the minimum of the collisional mobility in Fig. 1(c)).

In calculations illustrated in Fig. 1, we have not considered any energy losses due to electron-wall interactions [$\alpha_e = 0$ and $W = 0$ in Eq. (2)]. The dominant loss term for the electrons is the third term on the left-hand side of Eq. (2). In previous calculations,^{13,15,20,21,31} where the anomalous diffusion of the electrons was governed by electron-wall collisions and Bohm like transport, the coefficient α_e involved in Eq. (2) was varied between 0.2 and 1.2 to obtain discharge current in agreement with experimental results. The maximum of electron mean energy ε was on the order of 30 eV, which corresponds to an electron temperature T_e of 20 eV ($T_e = 2/3k_B\varepsilon$). The calculated electron temperature was in agreement with results of fluid description of plasma-wall sheath models (assuming a Maxwellian EEDF), which predict that under secondary electron emission due to high energy electrons impacting channel walls, the sheath becomes space-charge saturated (SCS).^{14,32} A critical temperature T_{cr} can be associated to this regime, which is 18 eV for a boron nitride wall.³³ Due to the lack of measurements in the PPS[®]100-ML thruster, in the hybrid simulations, α_e was chosen in order to obtain electron temperature on the order of the critical temperature.

From that time, measurements of electron temperature have been performed for different HETs. Langmuir probes have been employed to determine the electron temperature from plasma potential measurements in a 2 kW-class HET working with xenon, for discharge voltage varying from 200 V to 700 V for boron nitride walls,³⁴ and for carbon-velvet walls.³⁵ The boron nitride is a material with a high SEE coefficient while the carbon-velvet is a non-emitting material. In the case of boron nitride, results show that the maximum of electron temperature can exceed by far the critical temperature predicted by plasma-wall sheath fluid models. Floating emissive probes mounted on the high-speed axial reciprocating probe (HARP) system have permit to determine the two-dimensional distribution of the electron temperature for the NASA-173Mv1 thruster with boron nitride wall materials. Measurements have been performed for xenon gas for a discharge voltage of 300 V, and for discharge voltages of 500 V and 600 V for xenon and krypton gases.^{36,37} Again the maximum of electron temperature exceeds the critical temperature. Particle-in-cell simulations of the plasma slap bounded by the two walls show that the EEDF is non-Maxwellian, the plasma sheath never reaches a SCS regime in steady state,^{38,39} and the electron temperature can exceed the critical temperature, as observed experimentally. Since no measurements of the electron temperature have been performed in the PPS[®]100-ML thruster, the electron temperature remains unknown. We have performed calculations for different α_e to examine the effect of electron temperature on numerical outcomes. As we increase α_e to typical values previously used, the maximum of electron energy decreases and the maximum of ionization frequency is shifted towards the anode plane. For same fitted anomalous mobility, because most of the ions now can see the total potential drop applied between the two electrodes, the most

probable velocity of the ion VDFs shifts towards the high velocity, in total contradiction with experiments. This discussion clearly indicates a need for electron temperature measurements in the PPS[®]100-ML thruster.

We have calculated the time-averaged ion VDFs for different axial positions along the laser beam axis. We have plotted in Fig. 2 the calculated and measured ion VDFs for four axial positions. We see that the measured and calculated peaks of ion VDFs correspond. The calculated and measured velocity dispersions, in contrast, differ in the region where ionization and acceleration layers overlap. A larger dispersion for $x = 0$ mm can be seen in the measurements, while it is not obvious in the calculations. Due to strong gradients near the exit plane, the calculated dispersion is very sensitive to the axial spatial resolution. We have taken a spatial resolution of 0.2 mm as in the experiments. It seems that the discrepancy has to be attributed to different thruster operation regime in the experiments and in the calculations. Especially, the relative position of the ionization and acceleration regions that explains the velocity dispersion is different. We have performed calculations with a simple particle test model (not shown here) where we impose a stationary ionization source term and electric field profiles, as in Ref. 40. We confirm that a weak displacement of the ionization peak towards the exterior (for a fixed electric field profile) increases the velocity dispersion. The thickness of the layer where the velocity dispersion is large is also moved towards the exterior. As a last remark, we do not notice a peak in the ion VDFs at low energy in the experiments as well as in the calculations, at this radial position. When charge exchange (CEX) occurs, low energy ions are created. In the acceleration layer, the neutral density N is about 10^{18} m^{-3} . In most favorable conditions for CEX collisions, the characteristic time $\tau_{CEX} = (k_{CEX}N)^{-1}$ is roughly $10 \mu\text{s}$ for 20 km s^{-1} ions. An estimation of the time τ of singly charged ions to cross the ionization and acceleration layers ($d \sim 3 \text{ cm}$) gives $\tau \sim 1.5 \mu\text{s}$, which is shorter than τ_{CEX} . The charge exchange collisions are thus negligible for the ions in the near plume region.

B. Time-varying quantities

In order to be able to experimentally acquire the time dependent ion VDFs, a $10 \mu\text{s}$ power break (zero current) was

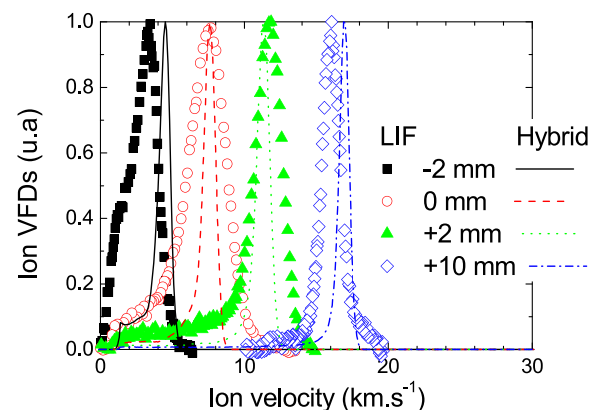


FIG. 2. Ion VDFs obtained by LIF measurements and calculated with the hybrid model along the laser beam axis. Conditions are the same as in Fig. 1.

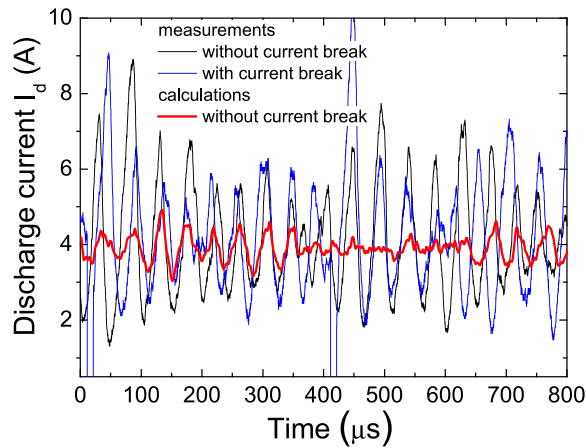


FIG. 3. Time evolution of the measured¹⁷ and calculated discharge current. Conditions are the same as in Fig. 1.

repeated every 400 μs to ensure repeatable conditions.⁹ Typically 1 million cycles are necessary to accumulate enough photons to obtain a reasonable ratio between signal and noise. In the calculations, we do not have interrupted the current. The electron anomalous mobility profile is the one previously computed and displayed Fig. 1(c). We have plotted in Fig. 3 the measured (with and without the interruption system) and the computed time evolution of the discharge current. The current peaks at $t=0$ and 400 μs that correspond ignition of the discharge. The high current is due to atom accumulation during the power break. If we compare the discharge current signal with and without the current break, we see that we reach a quasi-stationary regime 150 μs after the break, where the current oscillation is due to the periodic depletion of neutral atoms by high energy electrons.¹³ The oscillation frequency is closed to 20 kHz in the calculations and in the experiments. The main difference concerns the current standard deviation that is 1.6 A and 0.5 A in the measurements and calculations, respectively. The time-average discharge current is almost the same in the measurements and the calculations (~ 4 A).

The time and axial variations of the calculated electric field and ionization source term profiles along the laser beam axis are displayed Fig. 4 for several breathing period of the neutrals (the time evolution of the current is also plotted). In Fig. 4(a), the electric field strength oscillates as a function of time but the position of the maximum of electric field does not oscillate in space. The acceleration region is axially confined between $x = -2$ mm and $x = 8$ mm. Indeed, the calculated axial profile of the electric field is always very close to the time-averaged profile shown in Fig. 1(a). The origin of the electric field axial behavior can certainly be attributed to the fact that the anomalous electron mobility is time-independent in the simulations as it is obtained from time-averaged measurements of electric field. We show in Fig. 4(b) the ionization source term profile for identical conditions. The ionization source term is maximum ($\sim 1.4 \times 10^{24} \text{ m}^{-3} \text{ s}^{-1}$) when the discharge current is also maximum. Likewise, since the energy gained by the electrons is controlled by the electric field variation, the position of the maximum of the ionization source term does not move in axial direction. For same conditions, the time and axial

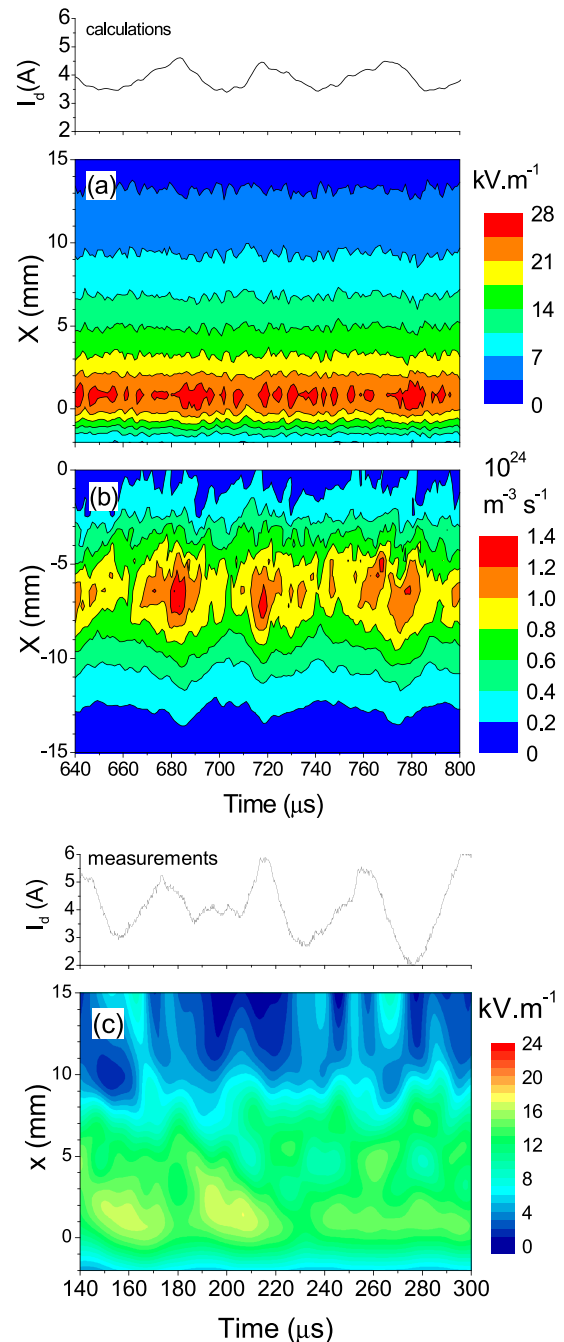


FIG. 4. Time and axial evolution of the (a) calculated electric field, (b) calculated ionization source term, and (c) measured electric field.¹⁷ The time evolution of the calculated and measured discharge currents is also shown. Conditions are the same as in Fig. 3.

variations of electric field deduced from measurements are given in Fig. 4(c), together with the time evolution of the discharge current. The method used to reconstruct the electric field profile should be taken with caution, especially inside the thruster channel. As mentioned in the introduction, the use of the Boltzmann method to access to the electric field profile from time-varying quantities is too complex in practice. A Lagrangian method has then been used in this study (more details are given in Ref. 9). Despite the approximations, we notice that the electric field profile varies not only in time but also in space. The maximum of electric field strength can occur outside the channel. In the results of Fig.

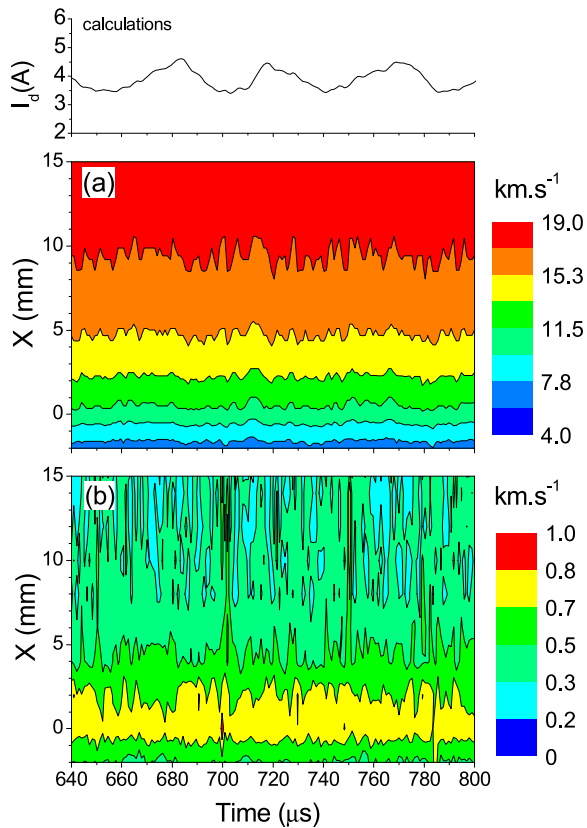


FIG. 5. Time and axial evolution of the calculated ion (a) most probable velocity and (b) velocity dispersion. The time evolution of the calculated discharge current is also shown. Conditions are the same as in Fig. 3.

4(c), we observe that an electric field front propagates from the outside towards the inside of the channel. We do not observe such propagation with the hybrid model. Previous calculations with a one-dimensional model have also exhibited the same trend.¹³ In the one-dimensional description of the thruster channel, as the discharge current increases, the ionization of neutral atoms starts in the interior of the channel and propagates towards the exit plane. We also observe the same situation with a fully kinetic description of two-dimensional geometry (axial and azimuthal directions).²⁵ This certainly can be attributed to the one-dimensional axial description of the neutral transport in both models.

We have plotted in Fig. 5 the most probable velocity and the dispersion of the ion VDFs profiles as a function of time and axial position. We define the dispersion as the full width at half maximum (FWHM) of the distributions. Since the ions can be considered in free fall, the ion VDFs are entirely controlled by the time and space variations of the ionization source term and electric field profiles. The profile in Fig. 5(a) does not oscillate in time and is very close to the time-averaged axial profile shown in Fig. 1(c). The maximum of velocity dispersion ($\sim 1 \text{ km s}^{-1}$) is concentrated near the channel exit. When one moves away from the exit plane, the velocity dispersion decreases to 0.2 km s^{-1} . The dispersion profile shown in Fig. 5(b) is also very close to the averaged in time profile we can construct from the ion VDFs plotted in Fig. 2. We have plotted in Fig. 6 the ion mean velocity (first order moment) and velocity dispersion obtained by Mazouffre and Bourgeois.⁹ As the calculated ion velocity dispersion, the

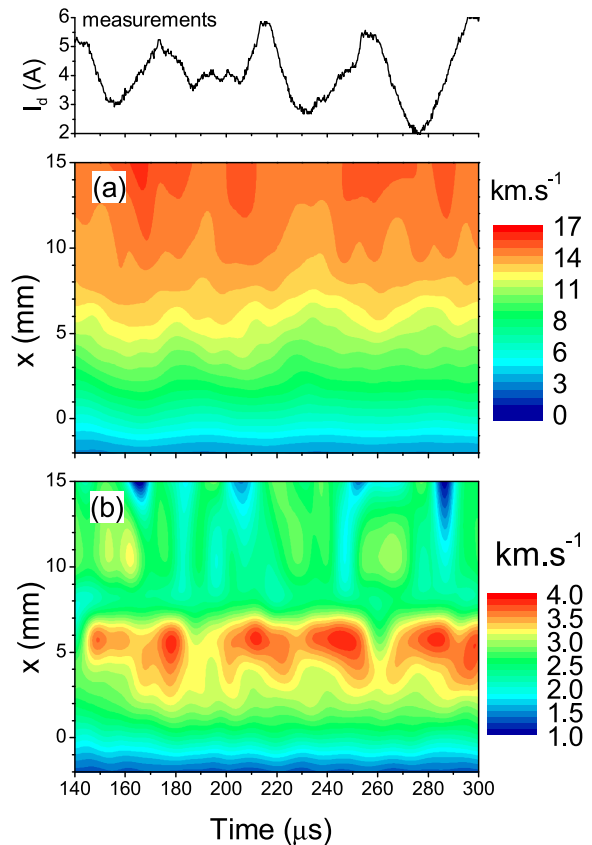


FIG. 6. Time and space evolution of the measured ion (a) mean velocity and (b) velocity dispersion.¹⁷ The time evolution of the measured discharge currents is also shown. Conditions are the same as in Fig. 3.

measured dispersion plotted in Fig. 6(b) does not vary much in time. However, we see that the peak of the dispersion in the measurement reaches four times the calculated maximum dispersion. The region where the dispersion is large (between $x = 3 \text{ mm}$ and $x = 7 \text{ mm}$) is shifted towards the outside, in comparisons with the calculations. This difference between experimental and calculated dispersion is consistent with the time-averaged ion VDFs displayed in Fig. 2. Unfortunately, we cannot use the Boltzmann method to construct the ionization frequency from measurements to see how the dynamics of ionization vary as the discharge current oscillates.

As we see in Fig. 3, the level of current oscillation is low in the calculations. We have also performed calculations with a discharge break of $10 \mu\text{s}$ by setting the discharge voltage to 0 V . Of course, the consequence is an amplification of the breathing mode oscillation regime by a strong ionization of the neutral atoms. As a consequence, the current peak reaches 8 A $60 \mu\text{s}$ after the break. In this particular situation, the region of strong electric field magnitude is still at the same position. The time-varying ion velocity dispersion profile is almost the same than in the situation without any current break. The discrepancies between experiments and calculations lead us to make two major remarks. From the time-varying measurements of the electric field profile, we can reasonably think that (1) the maximum of electron temperature also varies in time; it enforces the importance of electron temperature measurement and (2) the time-averaged anomalous mobility profile is a crude assumption. By setting

the anomalous mobility profile, we force the electric field profile to be spatially localized in the same region during all the thruster operation. We must emphasize that the reason for a maximum of electric field profile to be shifted from the region of strong magnetic field is however not clear. Raites and co-workers³³ report a situation where the time-averaged profile of the electric field shows a maximum in the near plume region for a 2 kW-class HET but at higher voltage. By comparisons with materials with low SEE, the shift of the maximum of electric field inside the plume was attributed to an enhancement of anomalous electron transport across the magnetic field region inside the channel due to an enhancement of the electron-wall conductivity. It is difficult from the simple analysis of ion VDFs we propose in this paper to conclude about the mechanism responsible for a time-varying anomalous mobility profile.

C. Self-magnetic field induced by the Hall current

We have calculated the Hall current density J_{Hall} in the PPS[®]100-ML thruster conditions to study the effect of the azimuthal current of the self-induced magnetic field. Neglecting the diamagnetic term, the Hall current density J_{Hall} can simply be expressed as:

$$\mathbf{J}_{\text{Hall}} = -en \frac{\mathbf{E}}{\mathbf{B}}, \quad (5)$$

where \mathbf{E}/\mathbf{B} is the azimuthal drift velocity of the electrons. We have plotted the time-averaged Hall current density profile in conditions of Sec. III B in Fig. 7. The Hall current density is maximum in the region where the azimuthal electron drift and the plasma density are large. The Hall current becomes negative when the electric field is reversed. The maximum of Hall current density in the conditions of this study reaches 0.12 MA m^{-2} . Koo and Boyd have calculated the Hall current density along the channel centreline for the P5 thruster for an electric power of 3 kW.¹⁶ The maximum reaches 0.2 MA m^{-2} . In the same conditions, Haas and Gallimore have characterized the Hall current density profile in two dimensions.⁴¹ In the exit plane, the maximum of current density varies from 0.1 MA m^{-2} , near the inner wall to 0.15 MA m^{-2} near the outer wall. For same positions, the magnetic field strength varies from 120 to 200 G. Following the procedure proposed in Ref. 41, we have integrated the force induced by the Hall current density ($J_{\text{Hall}} \times \mathbf{B}$ force) along the

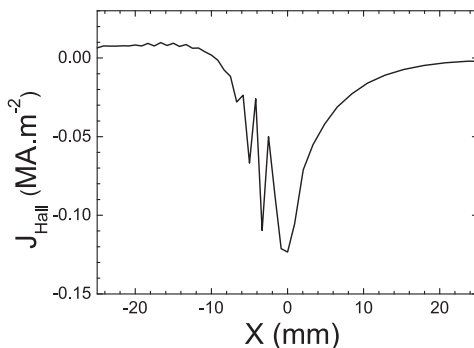


FIG. 7. Time-averaged profiles of Hall current density J_{Hall} along the axial position at a radial position of 4 mm from the internal wall.

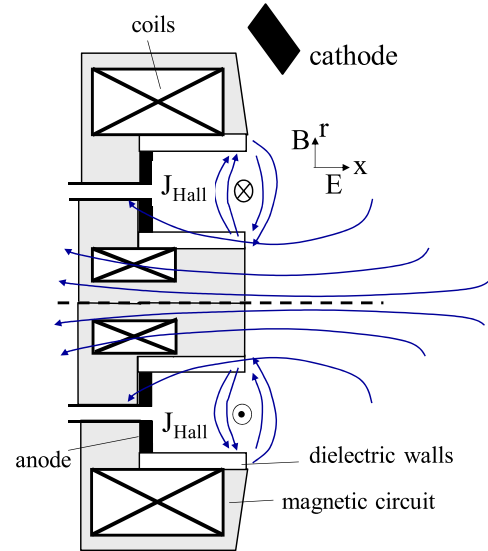


FIG. 8. Schematic of the magnetic system when a coil simulating the Hall current induced by the plasma is added.

axial position, considering a radial uniform profile. We obtain a force exerted by the Hall current of 77 mN, which is very close to thrust measurements for same thruster operation.⁴²

The qualitative influence of the Hall current on the magnetic field has been examined with the following method. We have positioned along the x axis a certain number of coils of 3 mm width whose current density is computed from the profile of Fig. 7. The FEMM software⁴³ has been used to calculate the magnetic field. As we observe on the drawing in Fig. 8, the magnetic field induced by the coil is positive inside the thruster channel and negative outside. Therefore, the total magnetic field strength (external + self-induced) increases inside the channel and decreases outside. Nevertheless, for the PPS[®]100-ML thruster, the calculated Hall current density is too low to modify the external magnetic field. The strength of the self-induced magnetic field is only a few G. For same plasma conditions, to obtain a clear effect of the self-induced magnetic field, the magnitude of the Hall current density must reach 1 MA m^{-2} .

IV. CONCLUSIONS

A detailed comparison between experimental and computed data has been performed for the PPS[®]100-ML thruster for time-averaged and time-varying quantities. The LIF spectroscopy technique has been used to accurately determine the axial ion VDFs at a given radial position. To overcome the weak signal-to-noise ratio in case of time-varying measurements, a photon counting technique has been successfully employed. Besides, a fast current break was used to get stable and repeatable discharge conditions. From time-averaged results, the ionization frequency and the electric field profiles have been determined by computation of high order moments of the Boltzmann's equation from the measured ion VDFs. This method cannot be used with time-dependent data. Instead, a Lagrangian method has been applied to determine the time-varying electric field profile from LIF measurements.

Calculations of the plasma properties have been performed with a two-dimensional hybrid model. In this model,

the electron transport is governed by fluid equations under the drift diffusion approximation, assuming a Maxwellian EEDF. The “anomalous” electron mobility that controls the electron diffusion across the region of strong magnetic field magnitude and low neutral density is adjusted from the electric field profile deduced from time-averaged LIF measurements. The transport of singly charged ions and neutral atoms is described with a particle method. This method permits to calculate the ion VDFs at a given radial and axial position for comparison with experimental results.

First, comparisons have been carried out for time-averaged quantities. Calculated and measured ion VDFs show charge exchange collisions are negligible in the channel exhaust region of a HET. If the calculated ion most probable velocity profile can match the experimental results, we have seen that the dispersion of the ion VDFs differs. This can be attributed to a different spatial distribution of the ionization source term in the calculations. Indeed, in the experiments, the peak of the ionization is shifted towards the channel exhaust. The peak of the ionization of frequency calculated with the hybrid model assuming a Maxwellian EEDF is also two times lower than the ionization peak in the experiments.

Second, we have performed comparisons for time-varying quantities. Comparisons of the time evolution of the electric field profiles exhibit differences. Especially, in the calculations, the strength of the electric field oscillates in time during the discharge current oscillation but not in space as in the experiments. This is certainly due to the time-independent profile of “anomalous” electron mobility in the model. The calculated ion velocity dispersion does not oscillate in time, in agreement with the very similar dynamic between the ionization source term and the electric field profiles during the thruster operation. Finally, the magnetic field induced by the azimuthal current was found to be too low to modify the applied magnetic field.

More generally, this set of comparisons underlines the necessity to measure the electron temperature; with time-resolved diagnostics if possible. The question of the influence of the shape of the EEDF on thruster operation is also enforced. Work will continue in these two directions. The comparisons also underline that a simple approach considering a given time-averaged anomalous electron mobility is clearly not able to capture the time-varying operation of a HET.

ACKNOWLEDGMENTS

This work is performed in the frame of the joint-research program CNRS/CNES/Sncema/Universités No. 3161 “Propulsion par Plasma dans l’Espace.” G. Bourgeois benefits from a CIFRE PhD Grant (No. 286/2009).

¹E. Ahedo, *Plasma Phys. Controlled Fusion* **53**, 124037 (2011), and references therein.

²L. Garrigues, *Plasma Phys. Controlled Fusion* **53**, 124011 (2011), and references therein.

³W. A. Hargus, Jr. and M. R. Nakles, *IEEE Trans. Plasma Sci.* **36**, 1989 (2008).

⁴W. A. Hargus, Jr. and M. A. Capelli, *Appl. Phys. B* **72**, 961 (2001).

⁵N. Dorval, J. Bonnet, J. P. Marque, E. Rosencher, S. Chable, F. Rogier, and P. Lasgorceix, *J. Appl. Phys.* **91**, 4811 (2002).

⁶D. Gawron, S. Mazouffre, N. Sadeghi, and A. Héron, *Plasma Sources Sci. Technol.* **17**, 025001 (2008).

⁷S. Mazouffre, D. Gawron, V. Kulaev, and N. Sadeghi, *IEEE Trans. Plasma Sci.* **36**, 1967 (2008).

⁸S. Mazouffre, G. Bourgeois, L. Garrigues, and E. Pawelec, *J. Phys. D* **44**, 105203 (2011).

⁹S. Mazouffre and G. Bourgeois, *Plasma Sources Sci. Technol.* **19**, 065108 (2010).

¹⁰G. J. M. Hagelaar, J. Bareilles, L. Garrigues, and J. P. Boeuf, *J. Appl. Phys.* **93**, 67 (2003).

¹¹J. Pérez-Luna, G. J. M. Hagelaar, L. Garrigues, and J. P. Boeuf, *Plasma Sources Sci. Technol.* **18**, 034008 (2009).

¹²R. Spektor, *Phys. Plasmas* **17**, 093503 (2010).

¹³J. P. Boeuf and L. Garrigues, *J. Appl. Phys.* **84**, 3547 (1998).

¹⁴S. Barral, K. Makowski, Z. Peradynski, N. Gascon, and M. Dudeck, *Phys. Plasmas* **10**, 4137 (2003).

¹⁵G. J. M. Hagelaar, J. Bareilles, L. Garrigues, and J. P. Boeuf, *J. Appl. Phys.* **91**, 5592 (2002).

¹⁶J. W. Koo and I. D. Boyd, *Phys. Plasmas* **13**, 033501 (2006).

¹⁷M. K. Scharfe, N. Gascon, and M. A. Cappelli, *Phys. Plasmas* **13**, 083505 (2006).

¹⁸F. I. Parra, E. Ahedo, J. M. Fife, and M. Martinez-Sanchez, *J. Appl. Phys.* **100**, 023304 (2006).

¹⁹I. G. Mikellides, I. Katz, R. R. Hofer, D. M. Goebel, K. de Gris, and A. Mathers, *Phys. Plasmas* **18**, 033501 (2011).

²⁰J. Bareilles, G. J. M. Hagelaar, L. Garrigues, C. Boniface, J. P. Boeuf, and N. Gascon, *Phys. Plasmas* **11**, 3035 (2004).

²¹L. Garrigues, G. J. M. Hagelaar, J. Bareilles, C. Boniface, and J. P. Boeuf, *Phys. Plasmas* **10**, 4886 (2003).

²²J. Szabo, M. Martinez-Sanchez, and O. Batishchev, “Numerical modeling of the near-anode region in a TAL thruster,” in *Proceedings of the 36th AIAA Joint Propulsion Conference and Exhibit, Huntsville, AL* (American Institute of Aeronautics and Astrophysics, Reston, 2000), AIAA Paper-2000-3653.

²³F. Taccogna, R. Schneider, S. Longo, and M. Capitelli, *Plasma Sources Sci. Technol.* **17**, 044003 (2008).

²⁴H. Liu, B. Wu, D. Yu, Y. Cao, and P. Duan, *J. Phys. D* **43**, 165202 (2010).

²⁵J. C. Adam, A. Heron, and G. Laval, *Phys. Plasmas* **11**, 295 (2004).

²⁶A. I. Morozov and V. V. Savelyev, *Fundamentals of Stationary Plasma Thruster Theory*, Review of Plasma Physics Vol. 21, edited by B. B. Kadomtsev and V. D. Shafranov (Consultant Bureau, New York, 2000).

²⁷S. Tsikita, N. Lemoine, V. Pisarev, and D. M. Gresillon, *Phys. Plasmas* **16**, 033506 (2009).

²⁸L. Garrigues, J. Pérez-Luna, J. Lo, G. J. M. Hagelaar, J. P. Boeuf, and S. Mazouffre, *Appl. Phys. Lett.* **95**, 141501 (2009).

²⁹J. C. Adam, J. P. Boeuf, N. Dubuit, M. Dudeck, L. Garrigues, D. Gresillon, A. Heron, G. J. M. Hagelaar, V. Kulaev, N. Lemoine, S. Mazouffre, J. Pérez-Luna, V. Pisarev, and S. Tsikita, *Plasma Phys. Controlled Fusion* **50**, 124041 (2008).

³⁰D. Piscitelli, A. V. Phelps, J. de Urquijo, E. Basurto, and L. C. Pitchford, *Phys. Rev. E* **68**, 046408 (2003).

³¹L. Garrigues, G. J. M. Hagelaar, C. Boniface, and J. P. Boeuf, *J. Appl. Phys.* **100**, 123301 (2006).

³²E. Ahedo, J. M. Gallardo, and M. Martinez-Sanchez, *Phys. Plasmas* **10**, 3397 (2003).

³³Y. Raitses, I. D. Kaganovich, A. Khrabov, D. Sydorenko, N. J. Fisch, and A. Smolyakov, *IEEE Trans. Plasma Sci.* **39**, 995 (2011).

³⁴Y. Raitses, D. Staack, A. Smirnov, and N. J. Fisch, *Phys. Plasmas* **12**, 073507 (2005).

³⁵Y. Raitses, D. Staack, A. Smirnov, and N. J. Fisch, *Phys. Plasmas* **13**, 014502 (2006).

³⁶J. A. Linnell and A. D. Gallimore, *Phys. Plasmas* **13**, 093502 (2006).

³⁷J. A. Linnell and A. D. Gallimore, *Phys. Plasmas* **13**, 103504 (2006).

³⁸I. D. Kaganovich, Y. Raitses, D. Sydorenko, and A. Smolyakov, *Phys. Plasmas* **14**, 057104 (2007).

³⁹D. Sydorenko, I. Kaganovich, Y. Raitses, and A. Smolyakov, *Phys. Rev. Lett.* **103**, 145004 (2009).

⁴⁰D. Gawron, Ph.D. dissertation, Université d’Orléans, 2007 (in French).

⁴¹J. M. Haas and A. D. Gallimore, *Phys. Plasmas* **8**, 652 (2001).

⁴²M. Touzeau, M. Prioul, S. Roche, N. Gascon, C. Pérot, F. Darnon, S. Béchu, C. Philippe-Kadlec, L. Magne, P. Lasgorceix, D. Pagnon, A. Bouchoule, and M. Dudeck, *Plasma Phys. Controlled Fusion* **42**, B323 (2000).

⁴³D. C. Meeker, Finite Element Method Magnetics version 4.2, 23 May 2008 Build, <http://www.femm.info/wiki/HomePage>.